Evidence of dilatant and non-dilatant damage processes in oolitic iron ore: P-wave velocity and acoustic emission analyses

Journal:	*Geophysical Journal International*
Manuscript ID:	GJI-07-0362.R2
Manuscript Type:	Research Paper
Date Submitted by the Author:	30-Sep-2008
Complete List of Authors:	wassermann, jérôme; Institut de Physique du Globe de Paris, Laboratoire Géomatériaux et environnement senfaute, gloria; INERIS amitrano, davide; Université Joseph Fourier, LGIT homand, françoise; Institut National Polytechnique de Lorraine, LAEGO
Keywords:	Attenuation, Compression, Cracked media, Earthquake-source mechanism, Fractures, Laboratory measurement, Microearthquakes, Microseismicity, P waves, Rheology, Rock fracture, Sedimentary basin

submitted to *Geophys. J. Int.*

Evidence of dilatant and non-dilatant damage processes in oolitic iron ore: P-wave velocity and acoustic emission analyses

J. Wassermann[1], G. Senfaute[2], D. Amitrano[3] and F. Homand[4]

[1]*Laboratoire Géomatériaux et environnement, Institut de Physique du Globe de Paris, France*

[2]*Institut National de l´Environnement Industriel et des Risques, France*

[3]*Laboratoire de Géophysique Interne et Tectonophysique, Université Joseph Fourier, Grenoble, France*

[4]*Laboratoire Environnement Géomécanique et Ouvrages, École Nationale Supérieure de Géologie, Nancy, France*

SUMMARY

Uniaxial and triaxial compression experiments were performed on oolitic iron ores to investigate damage processes. Most of these experiments included four indirect measurements of damage evolution, i.e. P-wave velocity and maximum amplitude received during pulse transmission experiments, elastic properties (apparent Young´s modulus and apparent Poisson´s ratio) and acoustic emission (AE) monitoring. The mechanical behaviour deduced from strain measurements is dilatant for some samples and non-dilatant for the other samples. However, variations in elastic properties indicate damage processes for all samples. AE source mechanism analysis shows two different microscopic damage processes: 1) for dilatant rock, the development of axial extensive microcracks as well as their interaction and coalescence lead to the formation of shear macroscopic discontinuities; 2) for non-dilatant oolitic iron ore, both compressive and shear micro-mechanisms take place and interact with macro-

scopic fractures. A particular consistency between the four types of measurements employed was observed.

Key words: damage – acoustic emission – dilatancy

1 INTRODUCTION

Mechanical loading of rocks induces irreversible microstructural changes such as pore crushing, microcrack nucleation and growth and grain compaction, which are referred to as damage processes. Such processes, when they occur suddenly, generate transient elastic waves known as Acoustic Emissions (noted AE, Evans 1979; Lockner 1993). Thus, AE constitute a practical tool for studying damage processes and have been widely used during uniaxial and triaxial compression tests of rocks (Scholz 1968b; Lockner et al. 1991; Cox & Meredith 1993; Lockner 1993; Zang et al. 1998; Lei et al. 2000; Amitrano 2003). From a macroscopic point of view, damage processes induce physical changes, such as modification of elastic properties (Lemaitre & Chaboche 1990). Damage processes thus induce wave velocity changes. Hence, the measurement of such parameters during the mechanical loading of rocks constitutes an indirect means for estimating damage evolution (Sayers et al. 1990).

In the case of rocks, in the early stage of deformation, extensive cracks nucleate and propagate parallel to the principal stress axis (Jaeger & Cook 1979; Reches & Lockner 1994). This phenomenon is well known and termed dilatancy: the strain measured perpendicularly to principal stress increases faster than the strain measured parallel to the principal stress. Some works have observed comparable anisotropic modifications using wave velocity measurements (Ayling et al. 1995; Stanchits et al. 2006). The onset of dilatancy is also related to the appearance of AE sources (Scholz 1968a; Lockner et al. 1991; Lockner 1993). The orientation of cracks can be inferred from AE source mechanism analysis (Zang et al. 1998). Wave velocity has also been used to monitor fracturing processes resulting from damage accumulation (Yukutake 1989; Chow et al. 1995; Rao & Kusunose 1995; Schubnel et al. 2003). In some cases, these measurements have been completed by amplitudes determined from pulse transmission experiments (Rao & Ramana 1992; Zang et al. 2000).

The stress level corresponding to dilatancy appears to dramatically vary with regard to the microstructure of the rocks and the confining pressure conditions (Rawling et al. 2002; Katz & Reches 2004). For porous rocks such as sandstone under high confining pressure, dilatancy may not appear and may instead be replaced by compaction due to grain crushing (e.g., Bésuelle et al. 2000).

Evidence of dilatant and non-dilatant damage processes in oolitic iron ore: P-wave velocity and acoustic emission

The goal of this study was to acquire a better understanding of iron ore damage processes that have occurred in the context of mine ground collapses. Uniaxial and triaxial compression experiments were performed on samples coming from different strata of an iron ore mine (the Tressange mine) located in Lorraine (eastern France). For studying the damage evolution, an extensive acoustic (i.e. AE monitoring and P-wave velocity measurements) and mechanical instrumentation was used during eight compression experiments. Here we present the results from six experiments including AE monitoring, P-wave velocity and mechanical measurements and two experiments including only mechanical measurements and AE monitoring. The mechanical measurements show a particular pattern indicating dilatant and non-dilatant mechanical behaviours of samples studied. Two experiments performed on dilatant and non-dilatant iron ores are presented here in detail, a particularly extensive sensor array (with 18 transducers) was used to determine damage micromechanisms.

2 EXPERIMENTAL PROCEDURE

2.1 Rock Description

The ferriferous formation in Lorraine (eastern France), dating from the Aalenian, is made up of a succession of sedimentary beds with varying iron content. Iron ore has been extracted from beds with high iron content (30 to 35 %). These iron ore beds, known by miners as the "Green", "Black", "Brown", "Grey", "Main Yellow", "Savage Yellow" and "Red" beds, from the base (deepest bed) to the top of the deposit, are separated by intercalated marl beds. An iron ore bed is composed of a sequence of three lithological formations materialized in a littoral environment (Bubenicek 1961; Teyssen 1989). There are, from the base to the top of the bed, an argillaceous and carbonated siltstone, an oolitic iron ore and a coarse shelled limestone. The jointed oolites of the oolitic iron ores that interest us, ovoid or spherical grains with a diameter of less than 1 mm, are made of goethite. The oolitic cortex is constituted of concentric layers most probably formed during biochemical processes (Burkhalter 1995; Konhauser 1998). The oolitic iron ore also contains other elements such as carbonated chips of shell tests, quartz grains and pieces of phosphatic bones (Bubenicek 1961). Centimetric black marl inclusions are also present, especially in the oolitic iron ore of the brown-iron layer. The iron ore grains (oolites and others) are cemented by a mixture of siderite, calcite and phyllosilicates in various proportions (Grgic 2001). One of the phyllosilicates, very ferriferous and green coloured, known as chamosite (Bubenicek 1970), is localized around grains or fills the entire space between oolites.

Table 1 presents the eight compression tests performed. Two samples came from a sub-vertical borehole (GM0203) drilled in intercalated marls with sub-horizontal bedding between the grey-iron layer and the brown-iron layer. The six iron ore samples came from two sub-horizontal boreholes drilled in oolitic iron ores. More precisely, these samples came from the G mine pillars of the grey-iron layer (GGP borehole) and from the brown-iron layer (BGP borehole) in the Tressange mine. The bedding is sub-horizontal at the GGP borehole location. In the case of the BGP borehole location, a substantial reworking has disturbed the original sub-horizontal bedding. The oolitic iron ores tested here are very porous rocks with a porosity of about 30 % for both the grey-iron and brown-iron layers. The intercalated marls have a porosity of about 15 %.

2.2 Experimental Setup

2.2.1 Sample Instrumentation

Samples were cut into cylinders of 140 mm in length (L) by 70 mm in diameter (D). Particular attention was paid to the parallelism of the ends of specimens. In order to measure the local strains in the central part of the samples, six strain gauges of 20 mm in length, three in the axial direction and three in the transversal direction, were placed on the sample surface. To ensure efficient coupling of the strain gauges, a resin was used to cover the sample surface. Eighteen piezoelectric transducers of 8 mm in diameter (Nano 30) from Physical Acoustic Corporation (PAC) were coupled to the surface of the sample (Figure 1). Phenyl salicylate crystals glued transducers on the lateral surface of the sample; silicon grease was used for the transducers on both ends of the specimen. The spectral band-pass of the transducers ranges from 100 kHz to 1 MHz with a major resonant frequency at 300 kHz. Their piezoelectric ceramic component can vibrate only in a longitudinal direction. Three transducers worked as transmitters and were dedicated to P-wave velocity measurements. Fifteen therefore operated as receivers of acoustic signals and constituted a mini-seismic network. Once the sample was fully instrumented, it was placed between two stainless steel end-pieces, machined especially to accommodate two transducers. The upper end-piece included a spherical seat to ensure a vertical position of the whole system constituted by the rock sample and the end-pieces that was placed between the machine platens. In order to reduce the end-effects of the contact between the rock specimen and the machine platens, the sample was placed between steel end-pieces with a cross-section equal to D. The ratio "length (L) over diameter (D)" of specimens was set to a value of 2 to restrict the stress heterogeneity domain and to obtain stress homogeneity in the central part of the sample (Brown & Brady 1985).

2.2.2 Compression Machine

The axial load was applied by a servo-controlled loading frame. The 1000 kN capacity machine used was enslaved by a computer controlled hydraulic pump. A pressure sensor placed between the pump and the press piston allowed the load during the test to be measured. Two LVDT (Linear Variable Differential Transformers) located between the machine platens (Figure 2) measured the axial displacements during sample deformation.

2.2.3 Data Acquisition Systems

The mechanical data acquisition system comprised two distinct units. One was dedicated to strain measurements while the other controlled the machine via the valve of the hydraulic pump and registered the load and the displacements. All the mechanical measurements were recorded every 6 seconds.

The acoustic data acquisition system consisted of two chains (Figure 2). The first included the receivers connected to 40 dB pre-amplifiers (PAC) with a 50 kHz-1.8 MHz spectral band-pass and the analogical/digital card (Engineering Seismology Group Canada Inc., Hyperion system), which digitises the signals after pre-amplification at a sample frequency of 10 MHz and with 14-bit vertical resolution with an amplitude interval of $\pm$ 2.5 V for each channel. This chain also performed AE counting in a continuous manner. The acoustic data (AE event waveforms) were stored on the hard drive of a computer during the experiment when amplitude reached a value larger than a given threshold. The maximum frequency recording was about 5 events per second. After the determination of the noise maximum amplitude, the signal trigger was set to 50 mV. When signals of 7 channels of the sensor array exceeded the former threshold, the system triggered and the signal was recorded for a fixed duration of 409.6 μs. The second acoustic chain enabled P-wave propagation velocity measurements. It consisted of a pulse generator (PAC) connected to the three transmitters via a switching box. The pulse generator generated a negative pulse with a maximum amplitude of about -360 V. During this type of measurement, AE monitoring was not performed.

2.3 Test Procedure

Uniaxial tests were carried out at a $10^{-5}s^{-1}$ constant longitudinal strain rate. The loading consisted in successive loading-relaxation-unloading cycles, with increasing axial load until failure (Figure 3). The relaxation phase allows the release of delayed elastic strain and therefore an appropriate determination of the elastic modulus during the unloading phase with

reduced hysteresis.

P-wave propagation velocity measurements were performed in the axial direction (ray T1R15, Figure 1) and in two transversal directions (rays T2R2 and T3R10, Figure 1), before every axial load cycle, and then at two points of each cycle (Figure 3), at the end of each relaxation phase (points a_i, i = 1 to Ncycles, Ncycles is equal to the cycle number) and during the following loading phase at the same stress level (points b_i). The recording of the AE activity was performed during loading and cycles, unless while P-wave measurements were being carried out.

2.4 Data Analysis Methods

2.4.1 Mechanical Analysis

Longitudinal (ϵ_L), transversal (ϵ_T) and volumetric ($\epsilon_V = \epsilon_L + 2\epsilon_T$) strains were plotted versus axial stress (σ_1). The displacements measured between the machine platens were also used to monitor the behaviour associated with the macro-failure. Indeed, strain gauges cannot record the strains during this phase due to macroscopic fractures destroying the strain gauges. The apparent Young´s modulus (E_{app}) and the apparent Poisson´s ratio (ν_{app}) have been estimated by linear regressions performed at each unloading phase of the cycles.

$$E_{app} = \frac{\sigma_1}{\epsilon_L} \tag{1}$$

$$\nu_{app} = -\frac{\epsilon_T}{\epsilon_L} \tag{2}$$

Where $\sigma \rangle 0$ is compression and $\epsilon \rangle 0$ denotes shortening.

2.4.2 Acoustic Analysis

The signals recorded during the pulsing phase were analysed in order to determine the P-wave velocity. The arrival time (t_P) was manually determined (so-called picking) from the signal waveforms. Each pulse generates an electromagnetic signal in the system that is present on all the waveforms recorded during the P-wave velocity measurements. The time of this artefact allowed identification of the origin time (t_0) of the pulse. Thus, P-wave velocity (Vp) is deduced from the time-of-flight ($t_P - t_0$) of the P-wave and the distance between the receiver R and the transmitter T (d_{RT}).

$$V_P = \frac{d_{RT}}{t_P - t_0} \tag{3}$$

The greatest uncertainty in Vp determination depends on the accuracy in picking the arrival time of the P-wave. This is estimated to be less than 2 %.

Maximum amplitude of the signal received during the P-wave velocity measurements allowed us to monitor evolution of attenuation of the medium during compression tests.

Concerning AE event signals, the first arrival time and the end of the signal were automatically picked using a Short Time Average/Long Time Average algorithm (Allen 1978). Thus, an event is recognized between the first arrival time and the end picking or end of the waveform. The energy of AE event signals was determined between such pickings as follows:

$$E = \frac{1}{N_k} \sum_{k=1}^{n_k} \left(\sum_j {A_{jk}}^2 . \Delta t \right) \quad (4)$$

where E is the signal energy of one AE event (in $V^2.s$), N_k the quantity of channels where the event has been identified, A_j the amplitude values at each sampling time between P-wave pick and end-pick in Volts (V), and Δt the sampling pitch. We considered that the signal energy received at the sensors was proportional to the source energy released (Evans 1979; Lockner 1993). The transducer polarisation was checked beforehand. It is negatively polarised (i.e. negative oscillation corresponds to compressional first motion). Then, the polarity of the first pulse amplitude, which is right after the P-wave pick, was studied for each waveform in order to assess the first motion characteristics of each event and thus AE event source mechanisms (Satoh et al. 1990; Lei et al. 1992; Zang et al. 1998). If the majority of channels have compressional (see Figure 4) or dilatational first motions, the events can result from tensile sources or compressive sources respectively. In other instances, the sources can be associated with a shear mechanism. Signal to noise ratios (SNR) were used to check the accuracy in picking the P-wave arrival time and thus the first motion determination, and were determined as follows as a function of the middle noise:

$$SNR = A_{first} . \left(\frac{1}{N} . \sum_N A_{noise} \right)^{-1} \quad (5)$$

where A_{first} is the maximum amplitude of the first pulse right after P-pick, A_{noise} the amplitude of the signal before P-wave pick and N the number of amplitude points before P-wave pick. If the SNR is less than 2.5, the channel is not taken into account in the compressive first motion ratio calculation.

3 EXPERIMENTAL RESULTS

3.1 Mechanical Behaviour

Figure 5 shows the mechanical behaviours of samples coming from the grey-iron layer (sample GGP1-A2, see Table 1), the brown-iron layer (BGP2) and from different facies of the

intercalated marl layer (samples GM0203S1 and GM0203S2). Dilatancy is clearly observed on the volumetric strain curves of GGP1-A2 and GM0203S1 (Figures 5a and 5b), the relative volumetric strain becomes negative as compression goes on. For BGP2 and GM0203S2 samples (Figures 5c and 5d), the volumetric strain curves do not show any dilatancy, the relative volumetric strain remains positive with compression. The mechanical behaviours of uniaxially compressed GGP and BGP samples including extensive instrumentation (Table 1 and Figure 1) are detailed below. Figures 6a and 6b illustrate the mechanical behaviour of the GGP sample. In 6b, six loading-relaxation-unloading cycles were performed in the linear part of the differential stress-displacement curve. Longitudinal, transversal and volumetric strains were plotted versus differential stress (axial stress minus confining pressure) in Figure 6a. Four main phases can be identified (Jaeger & Cook 1979). Firstly, the phase where the curve is upwardly concave, which is attributed to the closure of pre-existent cracks; secondly, the linear part of the curve related to pure elasticity; thirdly, the behaviour becomes non-linear, the curve reaches a maximum (σ_M, about 31 MPa) corresponding to the initiation of the macro-failure that grew and sheared during the fourth phase. Several stress thresholds were graphically identified (Table 2): σ_{CC} determined on the stress-displacement curve, is the initial crack closure threshold. The other thresholds came from stress-strain curves. σ_C, σ_{LL} and σ_D are respectively the cracking initiation determined on the transversal stress-strain curve, the loss of linearity of the longitudinal stress-strain curve and the dilatancy threshold observed on the volumetric strain curve. The peak stress σ_M is the maximum stress determined on the stress-displacement curves. The appearance of non-linear behaviour on the lateral strain curve from the threshold σ_C is attributed to the initiation of the cracking, while the σ_{LL} threshold corresponds to the linearity loss observed on longitudinal behaviour; it is attributed to the coalescence of microcracks. The dilatancy appears at the σ_D stress threshold about 24 MPa, volumetric strain increases indeed clearly from σ_D. The cycles present linear and reversible unloading and re-loading phases, with a very slight hysteresis. It can be seen that each unloading phase was performed after the relaxation phase allowing, thereby the release of delayed elastic strain. Unloading phases were also performed until the half of the preceding maximum stress. Non-linearity could be seen if the unloading phases would be performed until a null stress. It may be observed slightly during the first and second cycles of BGP compression (Figure 5d). Linear regressions were performed along each unloading phase for all cycles in order to determine the apparent Young´s modulus (E_{app}) and apparent Poisson´s ratio (ν_{app}). They are plotted versus stress in Figures 7a and 7c. The stress range from which the linear regression was performed is indicated for each modulus value by horizontal bars. Apparent

Young´s modulus variations are lesser than the error estimate and can be considered as constant, whereas the apparent Poisson´s ratio clearly increases with stress.

The mechanical behaviour of the BGP sample is shown in Figures 6c and 6d. Stress is plotted as a function of transversal, longitudinal and volumetric strains on the one hand and as a function of displacements on the other hand. The BGP mechanical behaviour observed in Figure 6 illustrates the four phases described for the GGP sample. However, for BGP the fourth phase related to macro-failure growth was not fully observed, since the loss of sample strength occurred too quickly to be monitored by the machine. The kink of the transversal strain-stress curve near the peak stress (point k, Figure 6c) corresponds to the failure of transversal strain gauges due to the macroscopic fracture growth (Figure 11). The pre-existing crack closure phase was more pronounced for BGP than for GGP (Figure 6) and BGP strength was higher than GGP strength (see Table 2). The σ_C and σ_{LL} thresholds were easily identified for BGP. Dilatancy was not observed for the BGP sample. The seven cycles show linear and reversible unloading and re-loading phases with a very slight hysteresis. As for GGP compression, apparent Young´s modulus variations during BGP loading (Figure 7b) are lesser than error estimate and should be considered as constant. Concerning ν_{app} (Figure 7d), important errors are associated with the measures performed during the three first cycles before the σ_{CC} threshold, so no trend can be discerned. After the σ_{CC} threshold, it increases with stress. Table 3 shows the mean values of the mechanical characteristics for each tested sample.

3.2 P Wave Velocities And Attenuation

The middle values of P-wave velocities determined along the axial ray (T1R15 ray, see Figure 1) and transversal rays (T2R2 and T3R10, see Figure 1) for each sample are given in Table 3. The axial velocities appear to be slightly faster than the transversal velocities. The difference between the two transversal velocities of the BGP sample is not significant regarding velocity uncertainty, for GGP it can be attributed to the heterogeneities. The P-wave velocities of the GGP sample are faster than for the BGP sample. The evolution of P-wave velocity of the samples during uniaxial compression and that of maximum amplitude of signals received during these measurements performed at both points a_i and b_i (see Figure 3) of each cycle are shown in Figure 8a and 8b for GGP and in Figures 8c and 8d for BGP. The attenuation was estimated through the maximum amplitude of the received signal. Normalized velocity ($Vp/Vp_{(\sigma=0)}$) and maximum amplitude ($Am/Am_{(\sigma=0)}$) are plotted versus stress. Stress thresholds are also given on the X-axis. On the whole, whatever velocity or maximum amplitude is considered,

the values at the end of the relaxation phase (points a_i) before unloading and values at an equivalent stress level during the re-loading phase (points b_i) are very close. This indicates that velocity and maximum amplitude do not vary during an unloading-reloading cycle.

As regards the GGP sample, the axial velocity measured along the ray T1R15 seems to be constant during the test, while transversal velocities (along T2R2 and T3R10 rays) decrease after cracking initiation (σ_C threshold) has been reached. Maximum amplitude variations are a little different, especially in the axial direction, where maximum amplitude increases until the σ_C threshold is reached and then becomes constant. In transversal directions, the maximum amplitude evolution is similar to those of transversal velocities.

Figures 8c and 8d show the evolution of normalized velocity and maximum amplitude for the BGP sample. Axial velocity increases slightly until cracking initiation (σ_C), while transversal velocities appear roughly constant during stress build-up. Concerning maximum amplitude, whatever direction is considered, it seems to decrease after stress reached the σ_{LL} threshold.

3.3 Acoustic Emissions

3.3.1 Acoustic Activity

The number of AE events identified for each sample compression test is given in Table 3. A set of 112 AE events were identified (P-wave picking performed) for the GGP sample and 160 for the BGP sample. Figures 9a and 9c superimpose AE activity (cumulative AE events) plotted versus displacements and stress-displacement curve respectively for the GGP and BGP samples. The cumulative energy of AE events during compression tests are also plotted in Figures 9b and 9d. It should be observed that, as for the GGP or BGP samples, loading-relaxation-unloading cycles are aseismic. AE is not observed unless stress has reached the previous maximum stress value revealing the Kaiser effect (Kaiser 1950; Goodman 1963). Concerning the GGP sample, AE activity is very low before stress has reached σ_{CC}. It increases after that stress level in a monotonous manner until peak stress, except between σ_{LL} and the onset of the non-linear pre-peak phase of the stress-displacement curve where it decreases slightly. During macro-failure growth beyond the strength peak (σ_M) and during macro-discontinuity shearing, the AE activity increase is stronger and includes the most energetic AE events. With regard to the BGP sample (Figures 9c and 9d), AE activity is higher than for the GGP sample during the pre-existing crack closure phase (prior to the σ_{CC} threshold); it shows a notable decrease during the linear phase of the overall mechanical behavior (linear part of the stress-displacement curve). The energy level of these AE events is low. AE activity increases strongly during the non-linear part of the differential stress-displacement curve then,

the more stress approaches σ_M, the more it becomes stronger and results in very energetic AE events.

3.3.2 First Motion Analysis

Compressive first motion ratios were determined for each AE event. Figure 10a shows its evolution during the GGP uniaxial compression test (see the stress thresholds on the X-axis). The first phase of the mechanical behaviour delimited by the σ_{CC} threshold includes events with a low compressive first motion ratio (less than 30 %) corresponding to compressive mechanisms and events with more than 70 % of compressive first motion related to extensive mechanisms. During the second phase, the linear part of the behaviour between σ_{CC} and σ_C (superimposed on σ_D in this figure) the majority of events includes a high compressive first motion ratio due to pure extensive mechanisms and also, in lesser proportion, a medium one caused by shear mechanisms. After the cracking initiation threshold (σ_C superimposed on σ_D), a mixed first motion dominated with a medium compressive first motion ratio, hence shear is the most important mechanism.

Concerning the BGP sample, the compressive first motion ratios are plotted in Figure 10b. Compression is associated with the high compressive first motion ratio blank that marked the absence of pure extensive mechanisms. BGP events that indeed include mainly a low (less than 30 %) and medium (between 30 % and 70 %) compressive first motion ratio, are distributed respectively during the first phase of mechanical behaviour (prior to σ_{CC}) and after cracking initiation (from the σ_C threshold). During the first phase, AE source mechanisms are mostly compressive. After σ_C threshold (superimposed on σ_{LL} threshold in this figure), shear mechanisms are dominant.

4 DISCUSSION

The first stage of the mechanical behaviour of GGP (Figures 6a and 6b) i.e. before the σ_{CC} threshold, where the concavity of the curve is upward, expresses a reduction in the axial compressibility of the rock. This behaviour is generally attributed to the closure of narrow pre-existing microcracks (Paterson 1978), the largest dimension of which is sub-orthogonal to the axial stress direction (σ_1). This hypothesis is reinforced on the one hand by the observation, during this first stage, of an increase in the P-wave velocity (Vp) and the maximum amplitude (Am) measured along the axial ray T1R15 (Figures 8a and 8b) and, on the other hand, by purely compressive sources (0 % of compressive first motions, Figure 10a). In the

case of the BGP sample, this first stage is also distinguished (Figures 6c and 6d). The assumption of microcrack closure is confirmed by purely compressive sources (Figure 10b) observed prior to the σ_{CC} threshold, but P-wave velocity (Vp) and maximum amplitude (Am) variations (Figures 8c and 8d) appear to not be affected by the microcrack closure. Pre-existing microcrack closure can be considered as a more or less reversible process that occurs only during the first phase of the mechanical behaviour i.e. when upward concavity of the stress-displacement curve is observed; according to Brace et al. (1966), pre-existing microcracks are being closed when the curve becomes linear. It can be seen that the non-linearity of the first phase of mechanical behaviour is only observed on stress-displacement curves both for GGP and BGP compressions and not on stress-strain curves. This may be explain by the nature of the measurements. Displacements were measured between the press platens (Figure 2). The displacement measurement is a measure of the axial strains that occur in the entirety of the sample and not only strains that take place in a central part of the sample. Indeed, longitudinal strain gauges are 20 mm long and measure strains along one-seventh of the longitudinal dimension of the sample. The closure of narrow pre-existing microcracks sub-orthogonal to the compression direction involves reduced strains that can be only clearly visible on the stress-displacement curves embracing the all closure processes.

During compression of very porous rocks such as oolitic iron ores, we expected pore crushing (Paterson 1978) that could also produce AE. Such an irreversible process (damage) could occur at low stress levels, especially if the pores are non-spherical inter-granular voids as in the rocks studied here. Grain rotations and translations could also occur (Kranz 1983) involving AE. Pore crushing is a pure compressive mechanism, whereas grain rotations and translations are related to shear mechanisms. These damage processes could also occur during the first stage of the mechanical behaviour and after the σ_{CC} threshold.

Several loading-relaxation-unloading cycles were performed in the linear part of the displacement-stress curves, six cycles for GGP and seven during BGP compression. Unloading phases, which correspond to the elastic response of the material, appear linear and reversible for both tests, even just after the loss of linearity (σ_{LL}) of the overall stress-longitudinal strain curves (Figure 6a and 6c), suggesting elastic deformation; these phases are mostly aseismic (Figures 9a and 9c). Indeed, we have seen that AE events can result from inelastic processes such as the creation of microcracks, pore crushing. Furthermore, Vp and Am measured before unloading (points a_i, Figure 8) and after re-loading (points b_i) are similar. Between cycles, a significant acoustic activity is recorded (Figures 9a and 9c), showing an inelastic process of deformation. Moreover, permanent strains are also visible when the unloading phase is linearly extrapo-

lated to a zero stress value (Figures 6a and 6c). Hence, the mechanical behaviour observed during uniaxial compression of GGP or BGP appears as a superposition of two deformation processes. One results from reversible processes such as elastic deformation of oolites and cement. The second embraces irreversible processes such as the initiation and interaction of microcracks, pore crushing, grain rotations and translations.

Variations in the apparent Poisson´s ratios (ν_{app}) during the GGP and BGP compression tests (Figures 7c and 7d) suggest damage processes. Concerning GGP compression, dilatancy observed on the volumetric strain-stress curve (Figure 6a) is attributed to the initiation of microcracks in extension, the largest dimension of which is sub-parallel to σ_1 (Brace et al. 1966; Jaeger & Cook 1979). This hypothesis of anisotropic damage characterized by such extensive microcracks is reinforced by the variations in Vp and Am (Figures 8a and 8b). Indeed, the axial velocity along the T1R15 ray is constant whereas the transversal velocities (rays T2R2 and T3R10) decrease strongly after the σ_C threshold, marking the opening of new voids such as microcracks (Goodman 1980). Oolitic iron ores are very porous sedimentary rocks and therefore pore crushing and readjustement of grains (ovoid oolites) should play an important role in irreversible deformation processes. However, as shown in Figure 10a, there is a small number of compressive AE sources registered (0 % of compressive first motions), AE sources before macroscopic manifestation of dilatancy (σ_D) have mostly pure extensive mechanism (100 % of compressive first motions), suggesting that the dominant damage process is more opening of new voids (microcracks) than compaction. This is mirrored in macroscopic measurements: there is no axial hardening (E_{app} seems to be constant, Figure 7a) and dilatancy is clearly observed (Figure 6a). Beyond the dilatancy onset, shear mechanisms are mostly registered (Figure 10a, from 30 % to 70 % of compressive first motions), in addition they correspond to very energetic AE events (Figure 9b) involving larger sources. Shear sources could result from the coalescence of axial extensive microcracks observed during the previous mechanical behaviour phase. Such a damage process has been observed in crystalline rocks under compression (e.g., Moore & Lockner 1995; Lei et al. 2000). Coalescence of extensive axial microcracks should form shear discontinuities that grow and lead to macroscopic failure (Figure 11). Reches & Lockner (1994) have modelled the propagation of such a fracture. It forms in a region of high extensive microcrack density. Then it grows through the coalescence of extensive microcracks and propagates with the creation of extensive microcracks at its tip.

For BGP compression, the apparent Poisson´s ratio increases beyond a stress value of 7 MPa, (Figures 7d), suggesting a damage process that takes place after the σ_{CC} threshold. Most of the AE events registered up to σ_C have a compressive mechanism (Figure 10b, from 0 % to 30

% of compressive first motions) suggesting pre-existing microcrack closure and pore crushing. Such processes lead to compaction in a direction sub-orthogonal to σ_1 that is mirrored partly in the macroscopic behaviour with positive volumetric strains during compression (Figure 6c) and total absence of dilatancy. This particular non-dilatant macroscopic behaviour was also observed during triaxial compression at low confining pressure of 5 MPa (Figure 5c). Associated damage process does not significantly affect the P-wave velocity and maximum amplitude (Figures 8c and 8d) and also the apparent Young´s modulus, which seems to be constant (Figure 7b). Beyond the σ_C threshold, shear mechanisms are dominant until failure (Figure 10b, between 30 % and 70 % of compressive first motions). As suggested by Escartin et al. (1997) in their study of non-dilatant brittle deformation of serpentinites through mechanical measurements and direct observations, shear mechanisms can involve dilatancy localized on irregularities on the fracture plane. But this localized dilatancy does not affect macroscopic mechanical behaviour as dilatancy induced by extensive axial microcracks. In sedimentary porous rocks, shear mechanisms should result from slides along inter-granular discontinuities and also from grain rotations and translations. AE events that have shear mechanisms are very energetic, as shown in Figure 9d, especially during the pre-peak phase where the stress-displacement curve becomes non-linear. We assume that such AE events were produced by sources larger than grain size i.e. along inter-granular discontinuities. These inter-granular discontinuities with shear mechanisms do not affect elastic wave propagation (axial and transversal velocities are constant, Figure 8c). They should coalesce to form macroscopic fractures leading to failure (Figure 12).

During GGP compression, we observed stress-induced velocity anisotropy through the decrease of transversal velocities (Figure 8a) and attenuation variations in axial and transversal directions (Figure 8b). This behaviour is associated on the one hand with pre-existing microcrack closure and, to a less extent, with pore crushing and with the opening of new voids such as extensive axial microcracks, on the other hand (Sayers et al. 1990). For GGP, where the bedding planes are subparallel to the compression direction, such an inherent anisotropy due to the formation of the rock influences deformation and damage processes (Chow et al. 1995; Gatelier et al. 2002). Bedding planes may constitute weakness planes subparallel to the compression direction in the GGP sample. Opening of extensive axial microcracks can occur on these planes. During GGP compression, stress-induced velocity anisotropy and dilatancy may be related to anisotropic damage processes (with opening of extensive microcracks, the largest dimensions of which are sub-parallel to σ_1). Concerning BGP compression, the measurements do not present any evidence of anisotropy. Since the bedding planes of this stratum

have been reworked, the BGP sample does not contain clear inherent anisotropy.

The presented results coming from independent measurements seem consistent for both sample compressions. Additional experiments (i.e. further uniaxial compressive tests for both grey-iron layer and brown-iron layer rocks) need to be performed to reinforce our hypothesis concerning the micro-mechanisms deduced from AE analysis and to state that the acousto-mechanical behaviours observed are representative for the rock types tested. The reproducibility of the acoustical observations should be statistically evaluated especially in the case of the heterogeneous sedimentary ferriferous formations studied here.

5 CONCLUSIONS AND PERSPECTIVES

Most of the experiments performed provided four indirect measurements of damage evolution, i.e. the P-wave velocity and maximum amplitude received during the pulse transmission experiment, elastic properties (apparent Young´s modulus and apparent Poisson´s ratio) and AE monitoring. Variations in elastic properties are consequences of microstructural changes (damage processes) that occur during compression. Dilatancy of the GGP sample, variations in the P-wave velocity and maximum amplitude and the analysis of AE source mechanisms lead to the hypothesis of the development of extensive axial microcracks, their interaction and coalescence constitute shear fractures that split the sample. For BGP non-dilatant rock, damage processes inferred from AE source mechanism analysis involve microscopic compressive and shear mechanisms that interact and lead to macroscopic fractures. Figure 13 shows a summary of the main interpretations. In both cases, GGP or BGP compression tests, microscopic processes deduced from AE analysis are consistent with macroscopic mechanical behaviour, P-wave velocity and maximum amplitude changes.

In order to complete these results, direct microstructural observations should reinforce the hypothesis concerning development of extensive axial microcracks observed during the GGP compression. Concerning BGP, since shear mechanisms are usually propagated in sedimentary rocks along the grain boundaries (Kranz 1983), direct observation could be difficult. Localization of AE sources and focal mechanisms deduced from first motion analysis could provide, as for seismic events, planes of possible shearing and hence the orientation of shear discontinuities.

ACKNOWLEDGMENTS

This research was carried out with the support of subsidies from the French Ministries for Industry and Research within the framework of GISOS (www.gisos.org). We express our gratitude to these organizations. We are grateful to P. Gaire and L. Schoumacker for their help during the experiments. We are also grateful to the two anonymous reviewers for their in depth review and constructive comments that helped to improve this work.

REFERENCES

Allen, R., 1978. Automatic earthquake recognition and timing from single traces, *Bulletin of the Seismological Society of America*, **68**(5), 1521–1532.

Amitrano, D., 2003. Brittle-ductile transition and associated seismicity: Experimental and numerical studies and relationship with the b value, *J. Geophys. Res*, **108**, 2044.

Ayling, M., Meredith, P., & Murrell, S., 1995. Microcracking during triaxial deformation of porous rocks monitored by changes in rock physical properties, I. Elastic-wave propagation measurements on dry rocks, *Tectonophysics*, **245**(3-4), 205–221.

Bésuelle, P., Desrues, J., & Raynaud, S., 2000. Experimental characterisation of the localisation phenomenon inside a Vosges sandstone in a triaxial cell, *International Journal of Rock Mechanics and Mining Sciences*, **37**(8), 1223–1237.

Brace, W., Paulding, B., & Scholz, C., 1966. Dilatancy in the fracture of crystalline rock, JJ geophvs, *Res*, **71**, 3939–3953.

Brown, E. & Brady, B., 1985. *Rock Mechanics: For Underground Mining*, Allen & Unwin.

Bubenicek, L., 1961. Recherches sur la constitution et la repartition des minerais de fer dans l'Aalenien de Lorraine, *Sci. de la Terre*, **8**, 5–204.

Bubenicek, L., 1970. *Géologie du gisement de fer de Lorraine*, Ph.D. thesis, Faculté des Sciences.

Burkhalter, R., 1995. Ooidal ironstones and ferruginous microbialites: origin and relation to sequence stratigraphy (Aalenian and Bajocian, Swiss Jura Mountains): Sedimentology, v. 42.

Chow, T., Meglis, I., & Young, R., 1995. Progressive microcrack development in tests on Lac du Bonnet graniteII. Ultrasonic tomographic imaging, *International Journal of Rock Mechanics and Mining Sciences and Geomechanics Abstracts*, **32**(8), 751–761.

Cox, S. & Meredith, P., 1993. Microcrack formation and material softening in rock measured by monitoring acoustic emissions, *International journal of rock mechanics and mining sciences & geomechanics abstracts*, **30**(1), 11–24.

Escartin, J., Hirth, G., & Evans, B., 1997. Nondilatant brittle deformation of serpentinites: Implications for Mohr-Coulomb theory and the strength of faults, *Journal of geophysical research*, **102**, 2897–2913.

Evans, A., 1979. *Fundamentals of Acoustic Emission*, chap. Acoustic emission sources in brittle solids, pp. 209–227, University of California, Los Angeles.

Gatelier, N., Pellet, F., & Loret, B., 2002. Mechanical damage of an anisotropic porous rock in cyclic triaxial tests, *International Journal of Rock Mechanics and Mining Sciences*, **39**(3), 335–354.

Goodman, R., 1963. Subaudible noise during compression of rocks, *Bulletin of the Geological Society of America*, **74**(4), 487–490.

Goodman, R., 1980. *Introduction to rock mechanics*, Wiley.

Grgic, D., 2001. *Modélisation du comportement à court et à long terme des roches de la formation ferrifère lorraine*, Ph.D. thesis, INPL, Nancy, France.

Jaeger, J. & Cook, N., 1979. Fundamentals of Rock Mechanics, 593 pp.

Kaiser, J., 1950. *An investigation into the occurrence of noises in tensile tests, or a study of acoustic phenomena in tensile tests*, Ph.D. thesis, PhD thesis.

Katz, O. & Reches, Z., 2004. Microfracturing, damage, and failure of brittle granites, *J. Geophys. Res*, **109**.

Konhauser, K., 1998. Diversity of bacterial iron mineralization, *Earth Science Reviews*, **43**(3-4), 91–121.

Kranz, R., 1983. Microcracks in rocks: a review, *Tectonophysics*, **100**(1-3), 449–480.

Lei, X., Nishizawa, O., Kusunose, K., & Satoh, T., 1992. Fractal structure of the hypocenter distributions and focal mechanism solutions of acoustic emission in two granites of different grain sizes, *Journal of Physics of the Earth*, **40**(6), 617–634.

Lei, X., Kusunose, K., Rao, M., Nishizawa, O., & Satoh, T., 2000. Quasi-static fault growth and cracking in homogeneous brittle rock under triaxial compression using acoustic emission monitoring, *J. Geophys. Res*, **105**(B3), 6127–6139.

Lemaitre, J. & Chaboche, J., 1990. *Mechanics of Solid Materials*, Cambridge University Press.

Lockner, D., 1993. The role of acoustic emission in the study of rock fracture, *International journal of rock mechanics and mining sciences & geomechanics abstracts*, **30**(7), 883–889.

Lockner, D., Byerlee, J., Kuksenko, V., Ponomarev, A., & Sidorin, A., 1991. Quasi-static fault growth and shear fracture energy in granite, *Nature*, **350**(6313), 39–42.

Moore, D. & Lockner, D., 1995. The role of microcracking in shear-fracture propagation in granite, *Journal of Structural Geology*, **17**(1), 95–114.

Paterson, M., 1978. Experimental Rock DeformationThe Brittle Field, 254 pp.

Rao, M. & Kusunose, K., 1995. Failure zone development in andesite as observed from acoustic emission locations and velocity changes, *Phys. Earth Planet. Inter*, **88**, 131–143.

Rao, M. & Ramana, Y., 1992. A study of progressive failure of rock under cyclic loading by ultrasonic and AE monitoring techniques, *Rock Mechanics and Rock Engineering*, **25**(4), 237–251.

Rawling, G., Baud, P., & Wong, T., 2002. Dilatancy, brittle strength, and anisotropy of foliated rocks: Experimental deformation and micromechanical modeling, *Journal of Geophysical Research (Solid*

Earth), **107**(B10).

Reches, Z. & Lockner, D., 1994. Nucleation and growth of faults in brittle rocks, *Journal of geophysical research*, **99**(B 9), 18159–18173.

Satoh, T., Nishizawa, O., & Kusunose, K., 1990. Fault development in Oshima Granite under triaxial compression inferred from hypocenter distribution and focal mechanism of acoustic emission, *Tohoku geophys. J.*, **135**, 241–250.

Sayers, C., Van Munster, J., & King, M., 1990. Stress-induced ultrasonic anisotropy in Berea sandstone, *International Journal of Rock Mechanics and Mining Sciences*, **27**, 429–436.

Scholz, C., 1968a. Microfracturing and the inelastic deformation of rock in compression, *J. Geophys. Res*, **73**(4), 1417–1432.

Scholz, C., 1968b. Experimental Study of the Fracturing Process in Brittle Rock, *Journal of Geophysical Research*, **73**(4), 1447–1454.

Schubnel, A., Nishizawa, O., Masuda, K., Lei, X., Xue, Z., & Guégen, Y., 2003. Velocity Measurements and Crack Density Determination During Wet Triaxial Experiments on Oshima and Toki Granites, *Pure and Applied Geophysics*, **160**(5), 869–887.

Stanchits, S., Vinciguerra, S., & Dresen, G., 2006. Ultrasonic Velocities, Acoustic Emission Characteristics and Crack Damage of Basalt and Granite, *Pure and Applied Geophysics*, **163**(5), 975–994.

Teyssen, T., 1989. A depositional model for the Liassic Minette ironstones (Luxemburg and France), in comparison with other Phanerozoic oolitic ironstones, *Geological Society London Special Publications*, **46**(1), 79.

Yukutake, H., 1989. Fracturing process of granite inferred from measurements of spatial and temporal variations in velocity during triaxial deformations, *J. Geophys. Res*, **94**, 15–639.

Zang, A., Christian Wagner, F., Stanchits, S., Dresen, G., Andresen, R., & Haidekker, M., 1998. Source analysis of acoustic emissions in Aue granite cores under symmetric and asymmetric compressive loads, *Geophys. J. Int.*, **135**(3), 1113–1130.

Zang, A., Wagner, F., Stanchits, S., Janssen, C., & Dresen, G., 2000. Fracture process zone in granite, *J. Geophys. Res*, **105**, 23651–23661.

Table 1. Synopsis of the laboratory experiments performed.

Sample	Sedimentary layer	Measurement type	Acoustic sensors	Channels for triggering	Pc (MPa)	$(\sigma_1 - Pc)_{max}$ (MPa)	AE events recorded
GGP1-A1	grey-iron	MA	8	1	0	27	1030
GGP1-A2	grey-iron	MA	8	1	0	28.4	1233
GGP2-2	grey-iron	MAVT	11	4	10	37.7	102
GGP	grey-iron	MAV	18	7	0	31.4	177
BGP	brown-iron	MAV	18	7	0	38.9	214
BGP2	brown-iron	MAVT	11	4	5	54.1	149
GM0203S1	intercalated marl	MAV	11	4	0	14.7	675
GM0203S2	intercalated marl	MAV	11	4	0	54.3	473

"MAVT" type corresponds to a Triaxial ("T") compression test including Mechanical ("M"), Acoustical ("A", AE monitoring) and P-wave Velocity ("V") measurements, "MAV" type includes the same measurements during uniaxial compression. "MA" type is for Mechanical ("M") and Acoustical ("A") measurements performed during uniaxial compressive test. If signals exceeded the trigger threshold (generally set to 50 mV) on at least the number of "Channels for triggering", the acoustical acquisition system triggered and the signal was recorded. The uniaxial compressive tests included six strain gauges whereas triaxial ones only four. Pc is the confining pressure.

Table 2. Stress thresholds (σ_{CC}, σ_C, σ_{LL}, σ_D, σ_M) for each sample.

Sample	σ_{CC} (MPa)	σ_C (MPa)	σ_{LL} (MPa)	σ_D (MPa)	σ_M (MPa)
GGP	5	11.4	18.6	24.2	31.4
BGP	5	11	15	-	38.9

σ_{CC} determined on the stress-displacement curve is the initial crack closure threshold. The other thresholds are deduced from stress-strain curves, σ_C, σ_{LL} and σ_D are respectively the cracking initiation determined on the transversal strain-stress curve, the loss of linearity of the longitudinal strain-stress curve and the dilatancy threshold observed on the volumetric strain curve. The failure stress σ_M is the maximum stress determined on the stress-displacement curve.

Table 3. Mechanical and acoustical characteristics and P-wave velocity for the two samples.

Sample	E_{app} (GPa)	ν_{app}	Vp_{axial} m/s	Vp^{top}_{trans} m/s	Vp^{bottom}_{trans}	AE events	b_e
GGP	29.2	0.28	4171	3981	4143	112	0.63
BGP	19.9	0.11	3160	3058	3031	160	0.51

E_{app} is the apparent Young´s modulus, ν_{app} the apparent Poisson´s ratio. Vp_{axial} is measured along T1R15 ray, Vp^{top}_{trans} along T2R2 transversal ray and Vp^{bottom}_{trans} along T3R10 transversal ray. An AE event is identified between P-pick and end-pick on at least 8 channels. b_e value is estimated from AE energy distribution ($Log(N) = c - b_e Log(E)$, where N is the number of AE events that have signal energy greater than or equal to E, c and b_e are constants, and E the AE event signal energy, see equation 4).

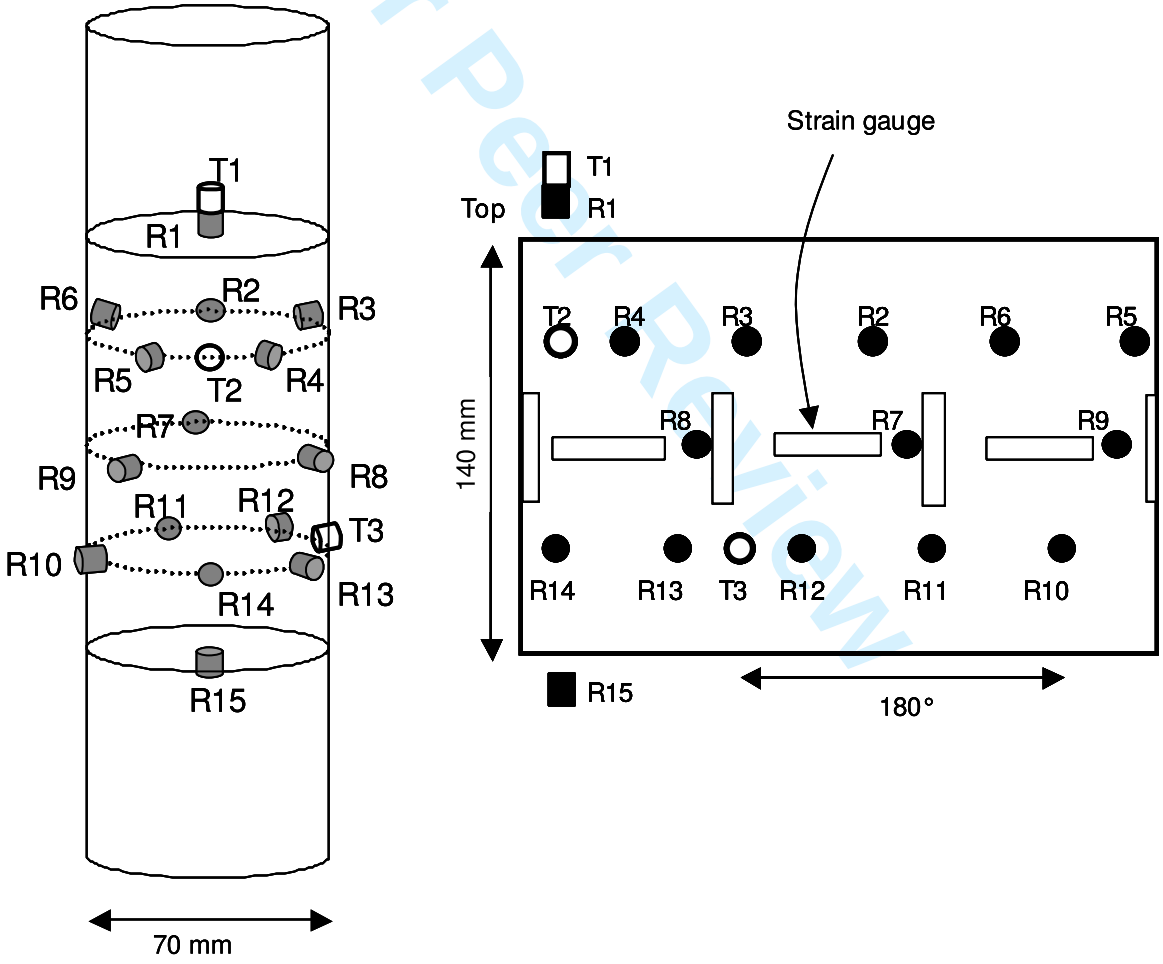

Figure 1. Sample instrumentation scheme. Strain gauges (rectangles in the central part of the sample) and piezoelectric transducers are glued on the sample surface. T transducers are transmitters and R are receivers.

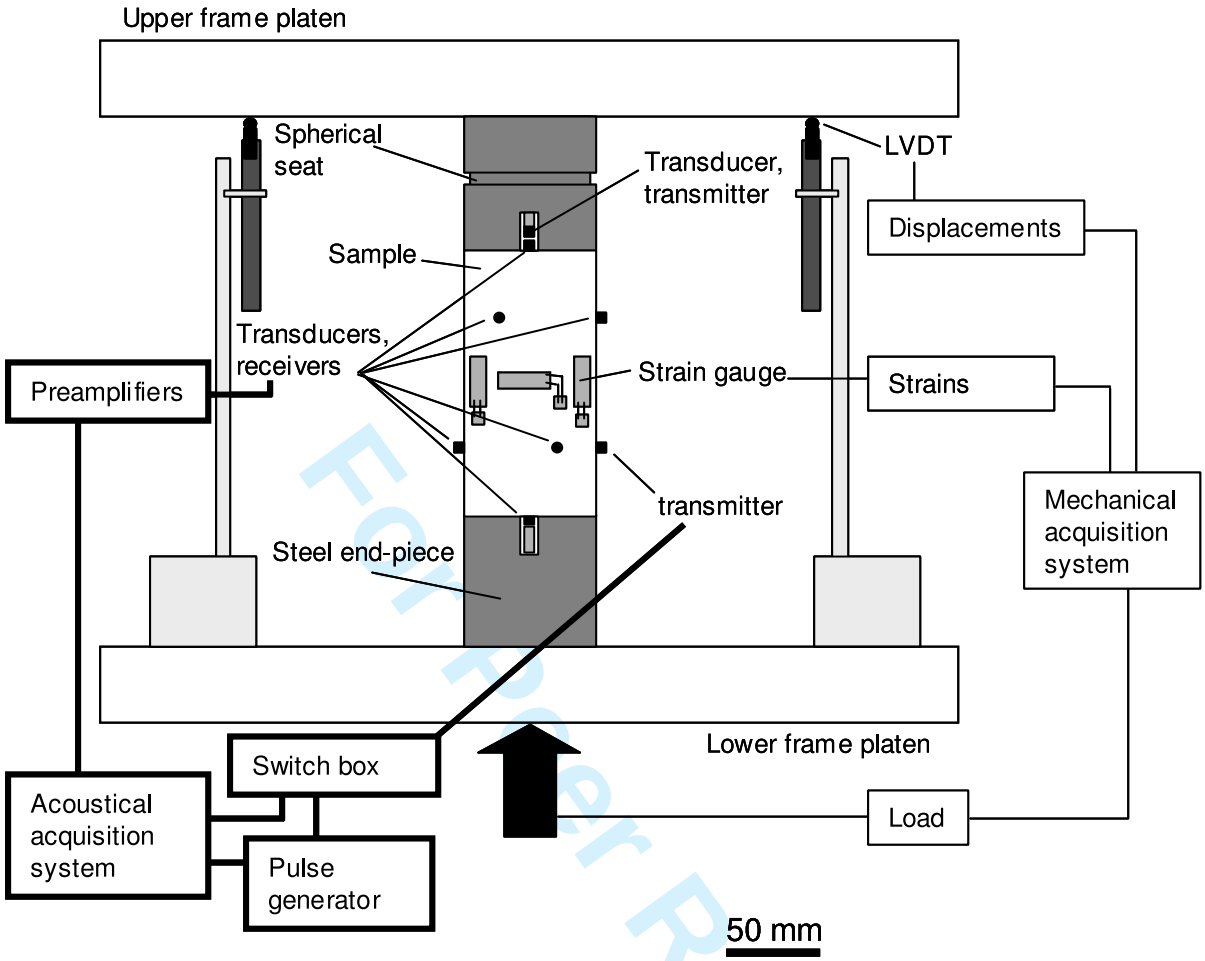

Figure 2. Experimental system scheme. Mechanical acquisition system includes six strain gauges glued on the lateral surface of the sample and two LVDT placed between the press platens. The acoustical acquisition system is constituted by transducers (3 transmitters and 15 receivers), which are coupled to the sample surface, preamplifiers, acquisition analogical/digital card, and also, for the pulse transmission experiment, a pulse generator and a switch box.

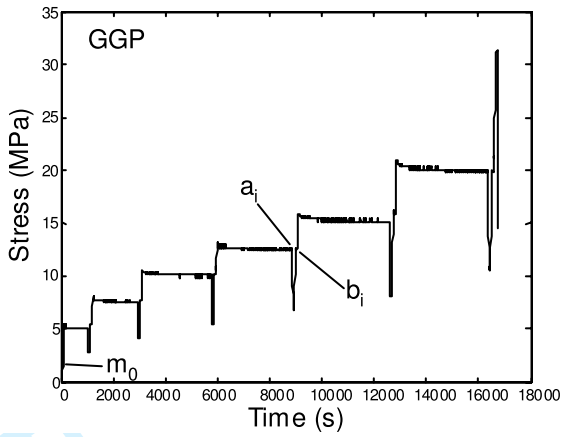

Figure 3. Loading history with loading-relaxation-unloading cycles. The stress is plotted versus time. Velocity measurements (in axial and transversal directions) were performed at points m_0, a_i and b_i (i: cycle number).

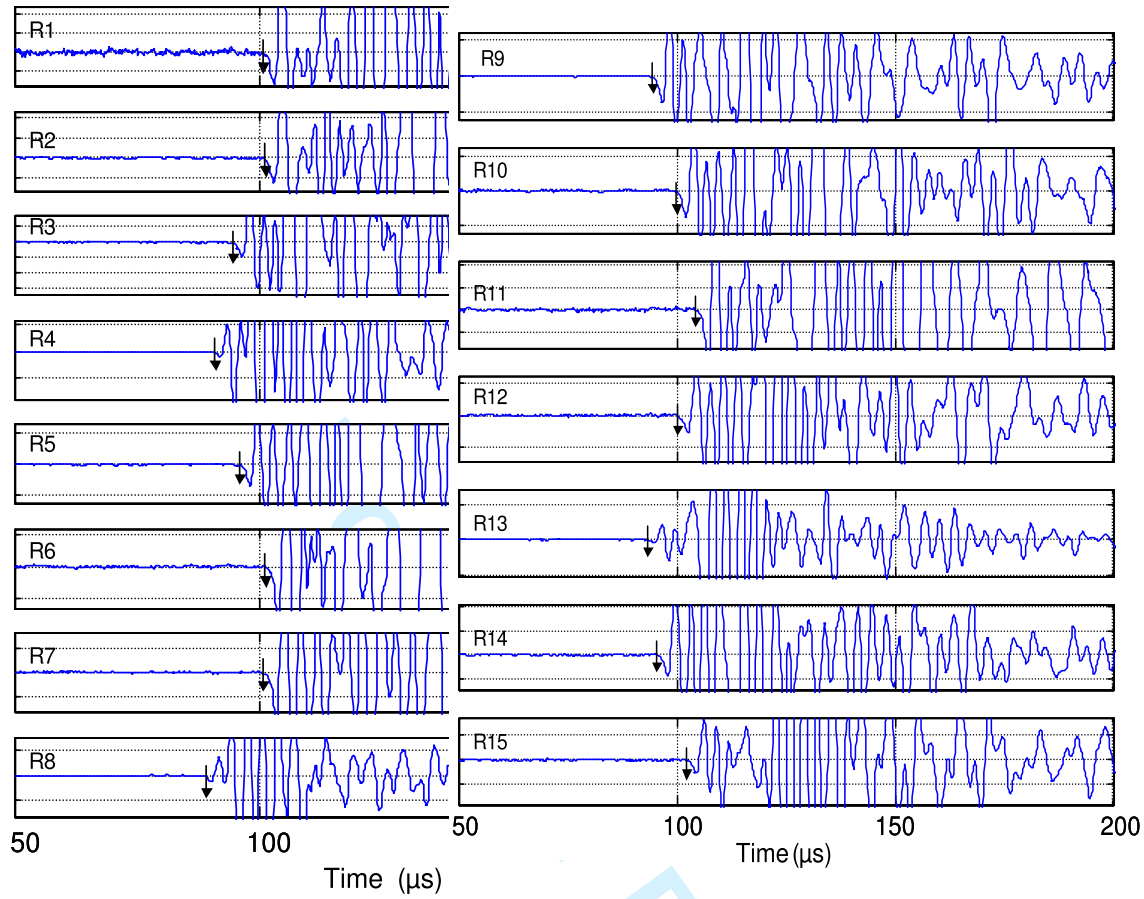

Figure 4. Enlargement of first motions of signal traces on 15 receivers (R1 to R15) of an AE event recorded during GGP compression test. The transducer polarisation is negatively polarised i.e. negative oscillation corresponds to compressional first motion. First motions showed here are all compressional. Hence, this event can result from a tensile source.

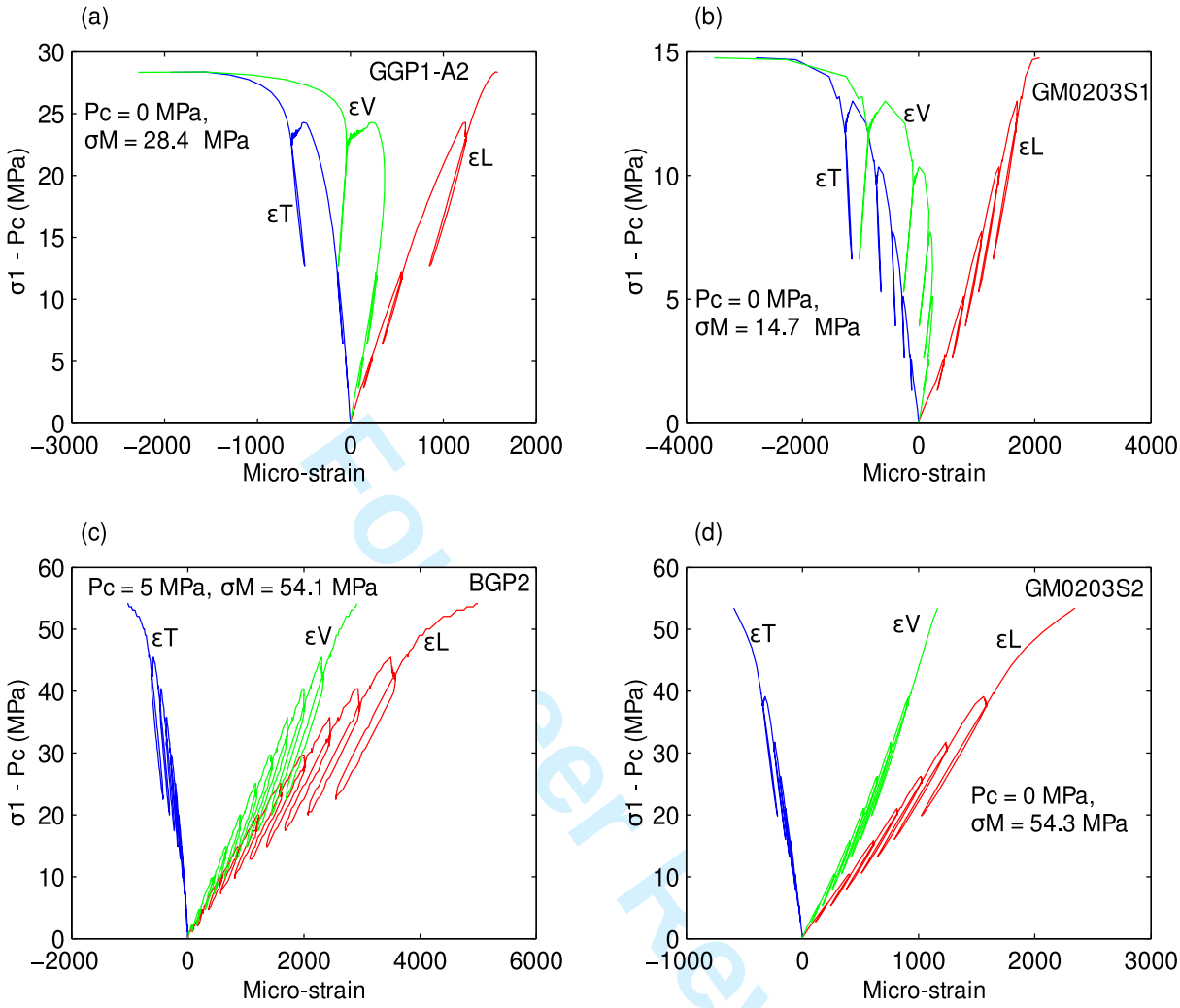

Figure 5. Mechanical behaviours of samples coming from different levels of the iron ore and intercalated marl beds. a) sample GGP1-A2 from the grey-iron layer; c) sample BGP2 from the brown-iron layer; b) and d) samples GM0203S1 and GM0203S2 from different facies of the intercalated marl layer. The differential stress ($\sigma_1 - Pc$, with Pc the confining pressure) is plotted versus transversal, longitudinal and volumetric strains, respectively, ϵ_T, ϵ_L and ϵ_V measured using strain gauges. σ_M is the maximum stress value.

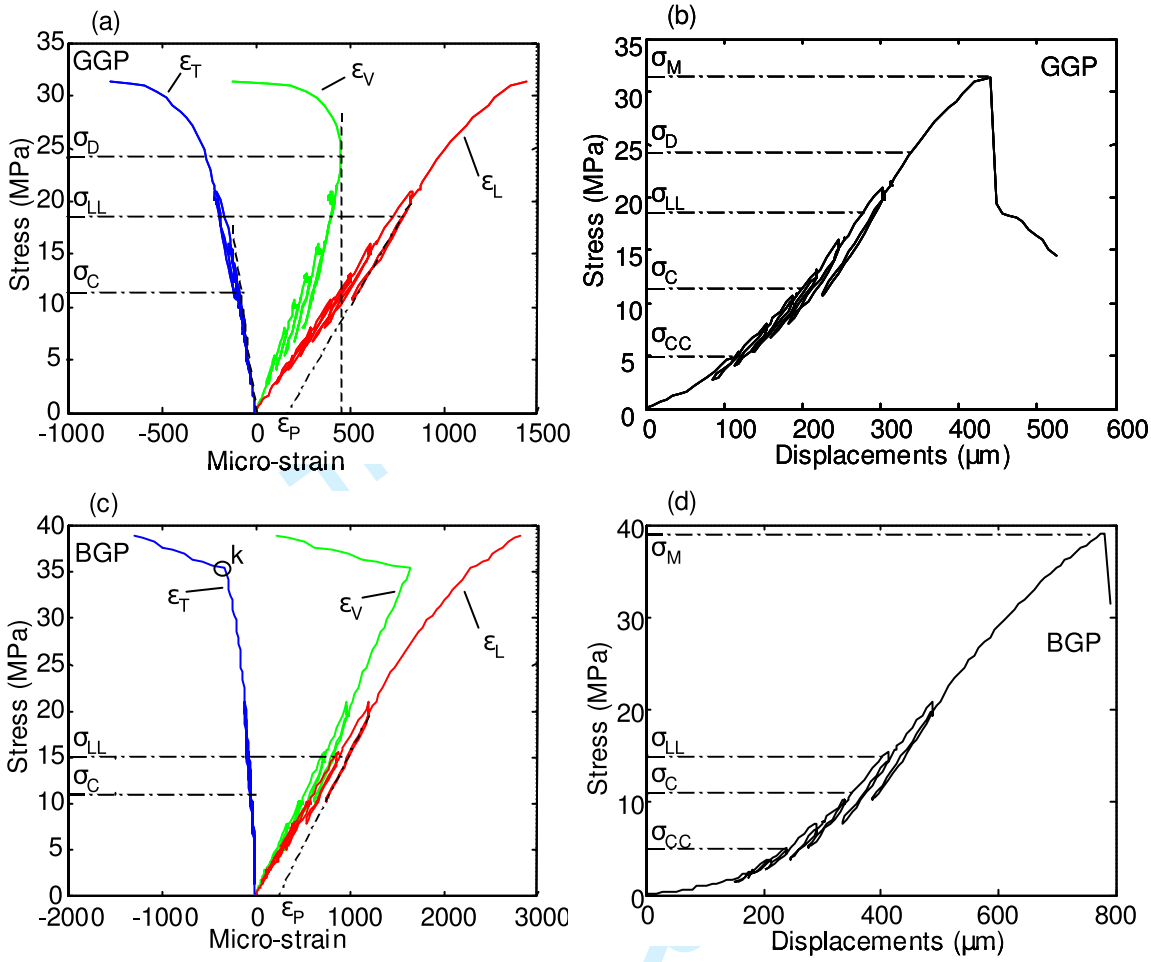

Figure 6. Mechanical behaviour of uniaxially compressed GGP (a and b) and BGP (c and d) samples. The stress is plotted versus transversal, longitudinal and volumetric strains, respectively, ϵ_T, ϵ_L and ϵ_V measured using strain gauges. Stress is also plotted as a function of displacements measured between the press platens. Stress thresholds were graphically determined. σ_{CC} determined on the stress-displacement curve is the initial crack closure threshold. The other thresholds came from stress-strain curves. σ_C, σ_{LL} and σ_D are respectively the cracking initiation determined on the transversal strain-stress curve, the loss of linearity of the longitudinal strain-stress curve and the dilatancy threshold observed on the volumetric strain curve. The peak stress σ_M is the maximum stress value determined on the stress-displacement curves. In c), the point k on the transversal strain-stress curve corresponds to the failure of transversal strain gauges that is mirrored in the volumetric strain-stress curve.

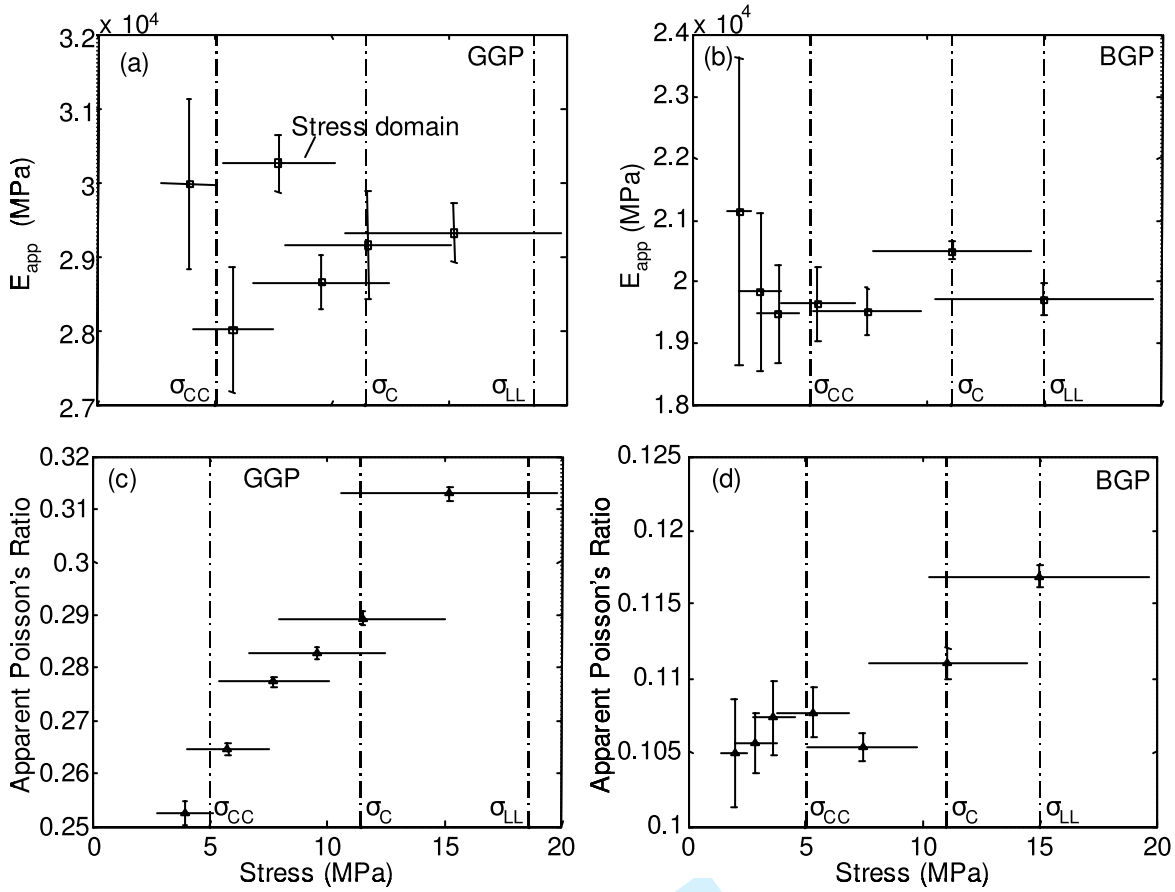

Figure 7. GGP elastic properties plotted versus stress: apparent Young´s modulus (E_{app}, a), and apparent Poisson´s ratio (c). BGP elastic properties plotted versus stress: apparent Young´s modulus (E_{app}, c) and apparent Poisson´s ratio (d). Each horizontal line represents the stress domain of each unloading phase where linear regression was performed to determine the modulus value and associated error (vertical segment). Stress thresholds σ_{CC}, σ_C and σ_{LL}, are reported on the X-axis.

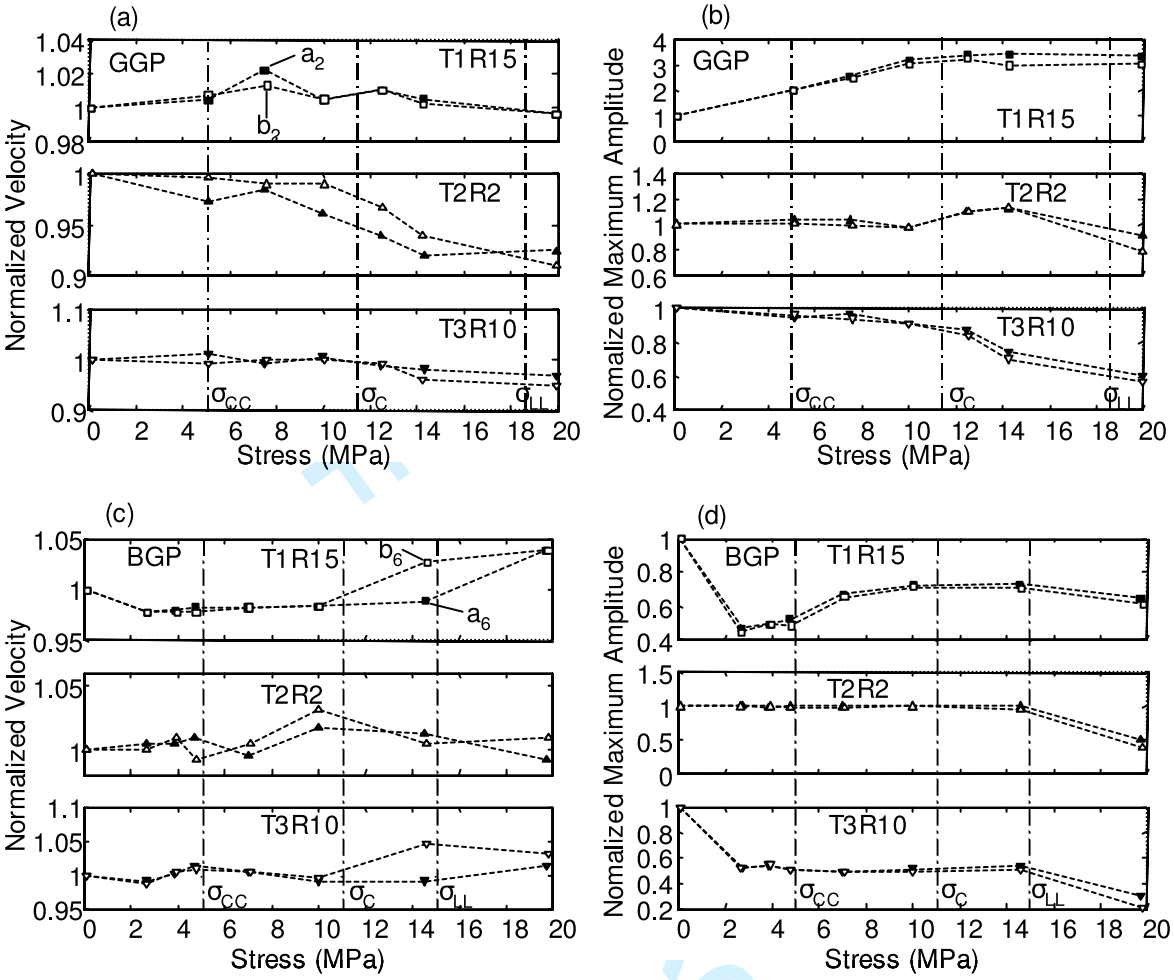

Figure 8. Normalized velocity ($Vp/Vp_{(\sigma_1=0)}$, a) and normalized maximum amplitude ($Am/Am_{(\sigma_1=0)}$, b) of the signal received during velocity measurements performed in compression of GGP. ($Vp/Vp_{(\sigma_1=0)}$) and ($Am/Am_{(\sigma_1=0)}$) are plotted versus differential stress for axial ray (T1R15) and transversal rays (T2R2 and T3R10). Velocity and maximum amplitude are both represented for measurement points a_i (end of relaxation phases, black markers) and points b_i (stress level equal to this a_i during the loading phases, white markers). Stress thresholds σ_{CC}, σ_C and σ_{LL} are reported on the X-axis. Normalized velocity (c) and normalized maximum amplitude (d) of the signal received during velocity measurements performed in compression of BGP.

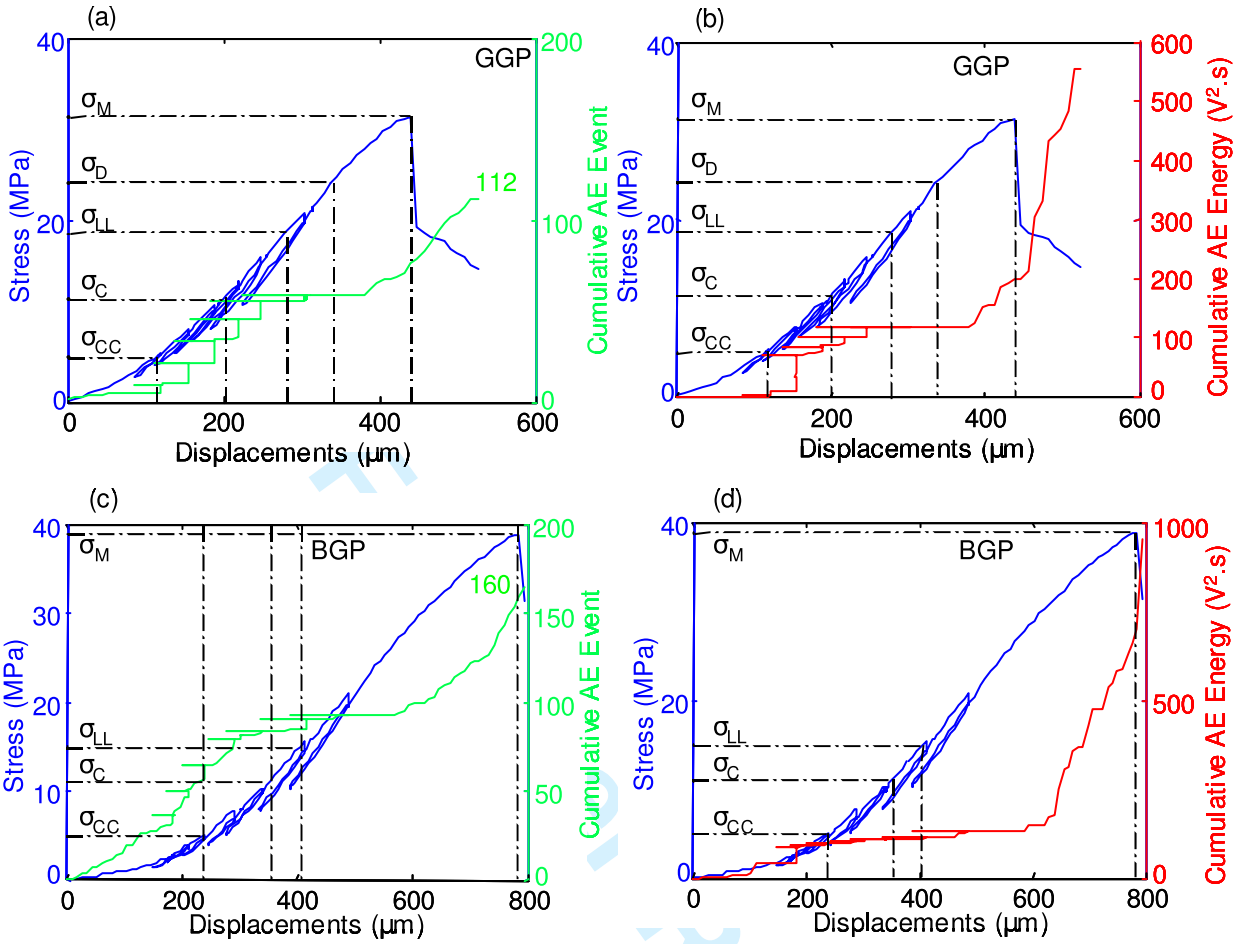

Figure 9. (a) Mechanical behaviour and acoustic activity during uniaxial compression of GGP. (b) Stress-displacement curve and AE energy during uniaxial compression of GGP. (c) Mechanical behaviour and acoustic activity during uniaxial compression of BGP. (d) Stress-displacement curve and AE energy for the BGP sample. Stress thresholds are reported on the Y-axis.

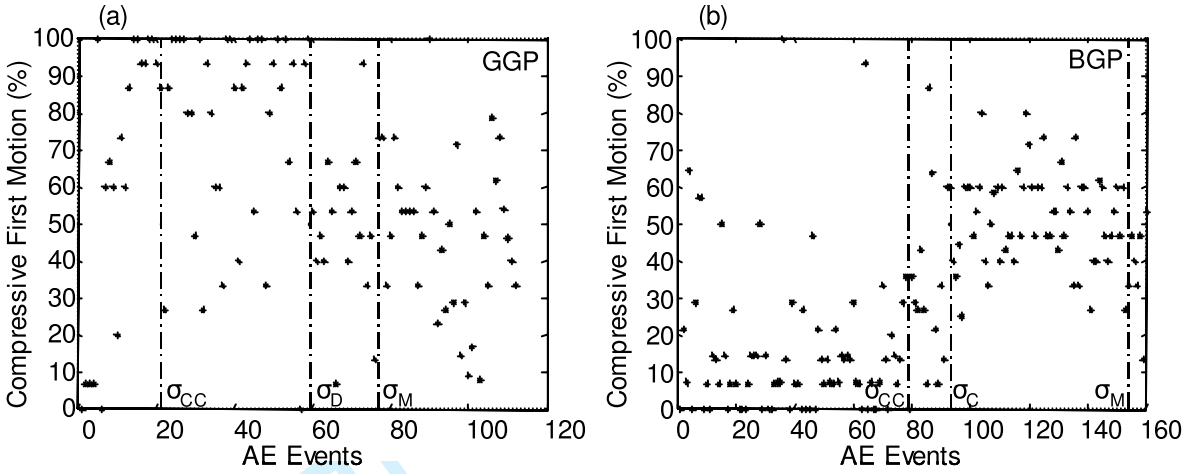

Figure 10. Compressive first motion ratio for each AE event recorded during GGP uniaxial compression (a) and during BGP uniaxial compression (b). Stress thresholds are reported on the X-axis. 100 % of compressive first motions correspond to pure extensive mechanism whereas 0 % of compressive first motions are related to pure compressive mechanism. Shear mechanisms induce AE events with compressive first motion ratio between 30 % and 70 %.

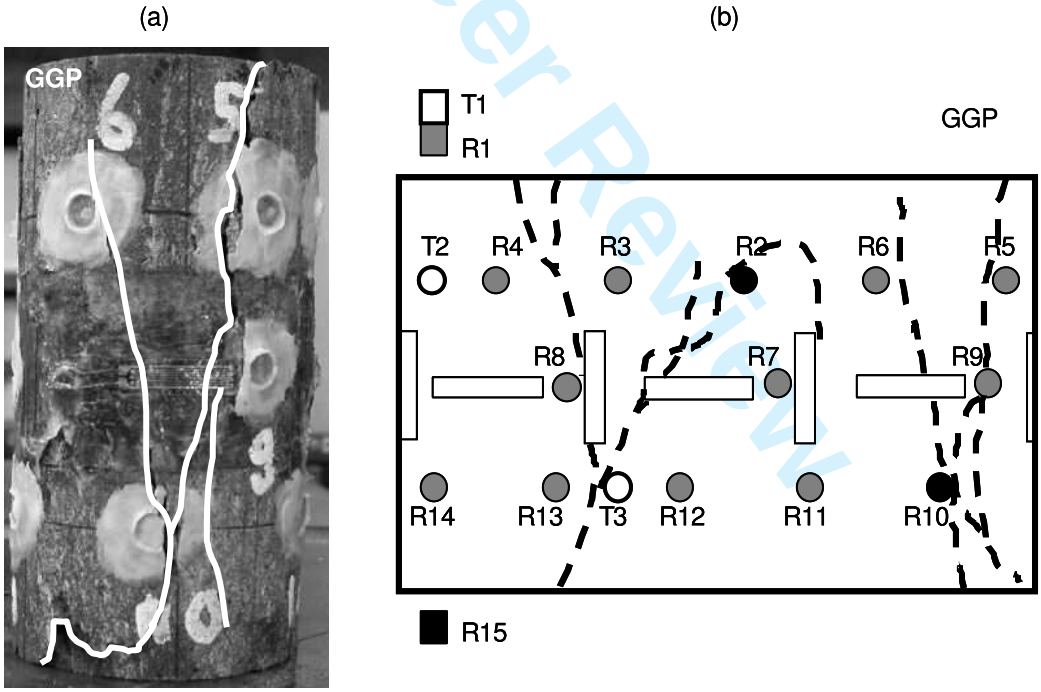

Figure 11. (a) Picture of the broken GGP sample showing irregular longitudinal splitting. (b) GGP sample scheme with strain gauges (rectangles in the central part of the sample) and piezoelectric transducer locations (circles on the lateral surface of the sample, rectangles at the both ends). The dashed lines represent the final macroscopic fracture traces.

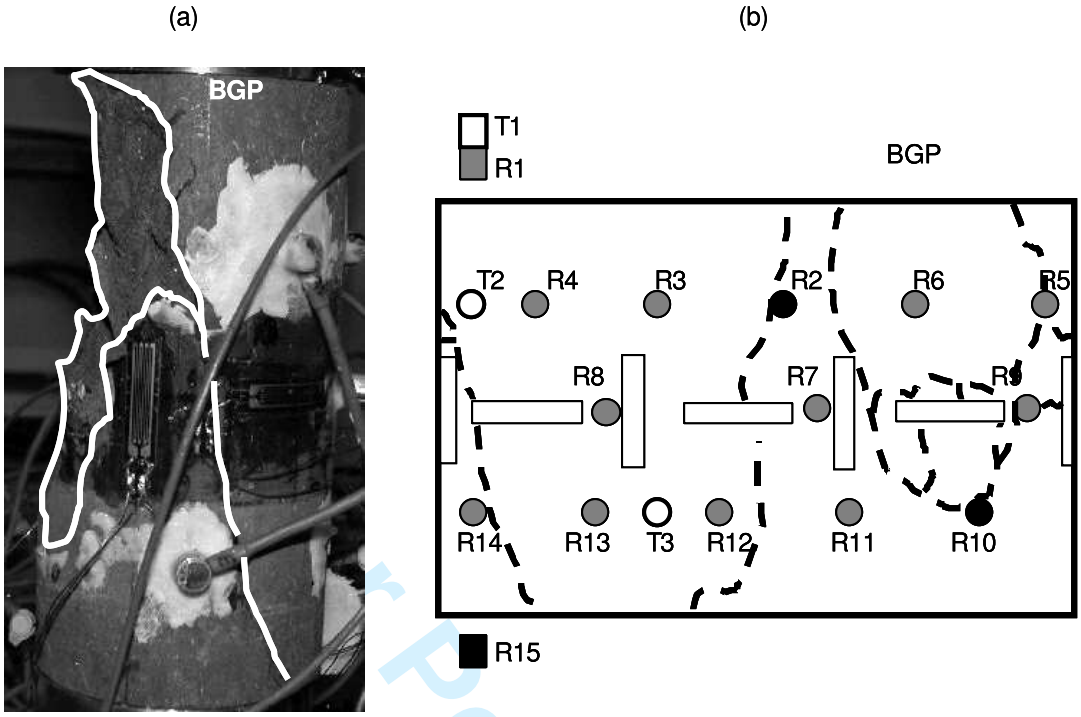

Figure 12. (a) Picture of the broken BGP sample. (b) BGP sample scheme with strain gauges (rectangles in the central part of the sample) and piezoelectric transducer locations (circles on the lateral surface of the sample, rectangles at the both sample ends). The dashed lines represent the final macroscopic fracture traces.

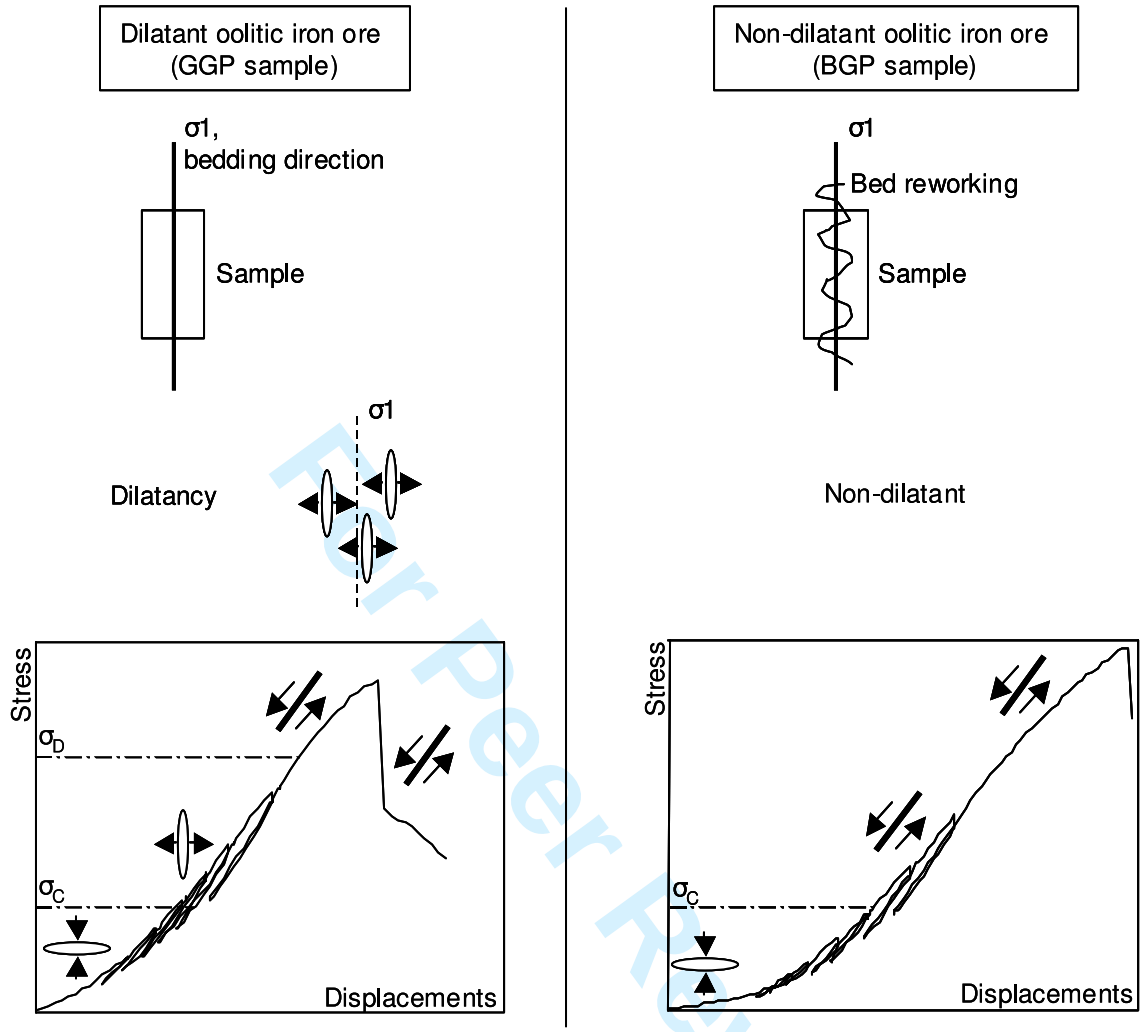

Figure 13. Diagram showing possible damage processes for dilatant and non-dilatant oolitic iron ores (respectively, GGP and BGP samples). Both sample deformations include damage processes. For the dilatant GGP sample, tensile cracking parallel to the σ_1 direction develops prior to the σ_D threshold. These extensive microcracks interact to form shear cracking. For the BGP non-dilatant sample, shear cracking develops beyond the σ_C threshold.